







First Clinical Investigation of Near-Infrared Window IIa/IIb Fluorescence Imaging for Precise Surgical Resection of Gliomas

Caiguang Cao , Zeping Jin, Xiaojing Shi , Zhe Zhang, Anqi Xiao , Junying Yang, Nan Ji , Jie Tian , *Fellow, IEEE*, and Zhenhua Hu , *Senior Member, IEEE*

Abstract—Objective: The near-infrared window II (NIR-II, 1000–1700 nm) imaging, including NIR-IIa (1300–1400 nm) and NIR-IIb (1500–1700 nm), outperforms the near-infrared window I (NIR-I, 700–900 nm) imaging in biological researches. However, the advantages of NIR-IIa/IIb imaging in human study are ambiguous. This study aims to apply the NIR-IIa/IIb imaging to glioma resection and evaluate their performance by using the developed imaging instrument and intraoperative image fusion method. **Methods:** A multispectral fluorescence imaging instrument that integrated NIR-I/II/IIa/IIb fluorescence imaging and an intraoperative image fusion method have been developed. Seven patients with grade III/IV glioma have been enrolled. NIR-I/II images of the tumor and NIR-I/II/IIa/IIb images of cerebral vessels were acquired with the administration of indocyanine green. Images were fused using the specialized fusion method to synchronously provide the distribution of the vessels and the surgical boundaries. **Results:** The NIR-IIa/IIb imaging was successfully applied to the clinic. High imaging resolution and contrast have been attained in the NIR-IIa/IIb spectra. Besides, capillaries with an apparent diameter as small as 182 μm were acquired using NIR-IIb imaging. Tumor-feeding arteries were precisely blocked and tumors were excised to the maximum extent for all patients. The blood loss volume during surgery was significantly reduced compared with the control group. **Conclusion:** The multispectral fluorescence imaging showed high performance, which led to a significant reduction in blood loss volume. **Significance:** The novel multispectral fluorescence imaging technology can assist surgeons in other vascular surgeries in the future.

Index Terms—Grade III/IV glioma, ICG, multispectral fluorescence imaging, NIR-IIa, NIR-IIb.

Manuscript received October 8, 2021; revised December 15, 2021; accepted January 9, 2022. Date of publication January 19, 2022; date of current version July 19, 2022. This work was supported in part by the National Key Research and Development Program of China under Grant 2017YFA0205200, in part by the National Natural Science Foundation of China (NSFC) under Grants 62027901, 81930053, 92059207, 81227901, and 81930048, in part by the Beijing Natural Science Foundation under Grant JQ19027, in part by the Strategic Priority Research Program of the Chinese Academy of Sciences under Grant XDA16021200, in part by the Zhuhai High-Level Health Personnel Team Project under Grant Zhuhai HLHPTP201703, in part by the Capital Characteristic Clinical Application Project under Grant Z181100001718196, and in part by the Innovative Research Team of High-Level Local Universities in Shanghai. (Caiguang Cao, Zeping Jin, and Xiaojing Shi contributed equally to this work.) (Corresponding authors: Nan Ji; Jie Tian; Zhenhua Hu.)

Caiguang Cao, Xiaojing Shi, and Anqi Xiao are with the CAS Key Laboratory of Molecular Imaging, Beijing Key Laboratory of Molecular Imaging, The State Key Laboratory of Management and Control for Complex

I. INTRODUCTION

FLUORESCENCE imaging has been widely investigated in the field of biomedical research due to its benefits, such as high sensitivity, high spatial resolution, real-time imaging ability, and operation convenience [1]–[6]. Imaging in the near-infrared window II (NIR-II, 1000–1700 nm) spectrum, especially in the NIR-IIa (1300–1400 nm) and NIR-IIb (1500–1700 nm) spectra provides deeper imaging depth and higher spatial resolution and it is demonstrated to be more adaptable for biological imaging [7]. That is mainly due to the photons in longer wavelength suffering lower tissue scattering and absorption [8], and the interference from tissue autofluorescence and ambient light is negligible [9]. Diverse NIR-IIa/IIb dyes have been synthesized over the past decades, their excellent performances for

Systems, Institute of Automation, Chinese Academy of Sciences, China, and also with the School of Artificial Intelligence, University of Chinese Academy of Sciences, China.

Zeping Jin and Zhe Zhang are with the Department of Neurosurgery, Beijing Tiantan Hospital, Capital Medical University, China, and also with the China National Clinical Research Center for Neurological Diseases, China.

Junying Yang is with the CAS Key Laboratory of Molecular Imaging, Beijing Key Laboratory of Molecular Imaging, The State Key Laboratory of Management and Control for Complex Systems, Institute of Automation, Chinese Academy of Sciences, China, and also with the Department of Hepatobiliary Surgery, Zhujiang Hospital, Southern Medical University, China.

Nan Ji is with the Department of Neurosurgery, Beijing Tiantan Hospital, Capital Medical University, Beijing 100070, China, with the China National Clinical Research Center for Neurological Diseases, Beijing 100070, China, and also with the Beijing Advanced Innovation Center for Big Data-Based Precision Medicine, School of Medicine, Beihang University, Beijing 100191, China (e-mail: jinan@bjtth.org).

Jie Tian is with the CAS Key Laboratory of Molecular Imaging, Beijing Key Laboratory of Molecular Imaging, The State Key Laboratory of Management and Control for Complex Systems, Institute of Automation, Chinese Academy of Sciences, Beijing 100190, China, with the School of Artificial Intelligence, University of Chinese Academy of Sciences, Beijing 100049, China, with the Beijing Advanced Innovation Center for Big Data-Based Precision Medicine, School of Medicine, Beihang University, Beijing 100191, China, and also with the Engineering Research Center of Molecular and Neuro Imaging of Ministry of Education, School of Life Science and Technology, Xidian University, Xi'an 710071, China (e-mail: tian@ieee.org).

Zhenhua Hu is with the CAS Key Laboratory of Molecular Imaging, Beijing Key Laboratory of Molecular Imaging, The State Key Laboratory of Management and Control for Complex Systems, Institute of Automation, Chinese Academy of Sciences, Beijing 100190, China, and also with the School of Artificial Intelligence, University of Chinese Academy of Sciences, Beijing 100049, China (e-mail: zhenhua.hu@ia.ac.cn).

This article has supplementary downloadable material available at <https://doi.org/10.1109/TBME.2022.3143859>, provided by the authors.

Digital Object Identifier 10.1109/TBME.2022.3143859

visualizing biomedical structures have been proved [10]–[12]. However, none of them have been deployed in the clinic yet, and the corresponding clinical benefits of NIR-IIa/IIb imaging are also needed to be explored.

Indocyanine green (ICG) is a fluorescent probe that has been approved by the US Food and Drug Administration (FDA). Recent studies have found it shows fluorescence in the shortwave infrared spectrum (SWIR, 1000–2000 nm) [13]. And SWIR imaging using it achieved real-time imaging of blood vessels and high contrast over the near-infrared window I (NIR-I, 700–900 nm) imaging in intravital animals [14]. Besides, our first-in-human study demonstrated that NIR-II imaging outperformed NIR-I imaging in clinical application [15]. Therefore, NIR-IIa/IIb imaging using ICG is also speculated to outperform the NIR-I imaging in clinical use.

Glioma is one of the most common primary tumors of the central nervous system [16], patients with grade III or grade IV glioma have a poor prognosis [17]. Surgical resection is considered to be an effective approach for treating this deadly disease [18]. During the surgery, it is crucial to precisely locate and block the tumor-feeding arteries and protect the important draining veins. However, since the aggressive vessel formation and abnormal vascular structure of grade III/IV glioma [19], [20], it is very hard to accurately identify the distribution of vessels around the tumor. Major bleeding resulting from mistakenly cutting off the feeding arteries increases the risk of cerebral infarction and ischemic stroke [21], [22]. Extended resection is used to stanch once the tumor-feeding arteries are not exactly blocked, whereas it inevitably damages the normal brain tissue and neuron system.

Currently, several methods have been used for clinical angiography. Preoperative imaging modalities, such as digital subtraction angiography, are used for diagnosing vascular-related diseases [23]–[25]. But these technologies suffer limitations of X-ray radiation and invasive inspection, and they are not widely used for real-time guidance during tumor resection [26]. Intraoperative imaging approaches like the NIR-I fluorescence angiography limited by the background fluorescence and tissue scattering are difficult to get high-resolution imaging. Therefore, an accurate and distinct indication of the vascular distribution alongside glioma resection is urgently needed. Based on our previous experiments, NIR-IIa/IIb imaging with ICG is an ideal intraoperative technology to break the above-mentioned obstacle and benefit the resection of grade III/IV glioma.

In this study, to apply the NIR-IIa/IIb imaging to glioma resection, and assess their advantages over NIR-I/II imaging in clinical application, an innovative instrument integrating NIR-I/II/IIa/IIb imaging was constructed with ICG used as the imaging probe. A corresponding intraoperative image fusion method was also developed. Seven patients with grade III/IV glioma were enrolled and the effectiveness of multispectral fluorescence imaging was assessed. The distribution of vessels around the tumor as well as the surgical boundaries were simultaneously delineated using the novel imaging system. All tumors were resected to the maximum extent without major bleeding. Overall, the NIR-IIa/IIb imaging was for the first time evaluated in the clinic and successfully used to guide the

glioma surgery. Cerebral vessels with a diameter as small as $182\ \mu\text{m}$ were clearly visualized. Besides, real-time blood flow perfusion was recorded in the NIR-II spectrum. Clinical results revealed the powerful use of multispectral fluorescence imaging especially imaging in the NIR-IIb spectrum. It may promote and assist other vascular-related surgeries in future clinical application.

II. METHODS

A. Development of the Multispectral Fluorescence Imaging Instrument and the Intraoperative Image Fusion Method

The multispectral fluorescence imaging instrument consisted of a combined multispectral imaging subsystem and a laser excitation subsystem. The detailed information of the imaging components and parameters was summarized in [Table I](#). The multispectral imaging subsystem was mainly composed of two fluorescence cameras. An electron-multiplying charge-coupled camera (ProEM-HS: 1024BX3, Teledyne Princeton Instruments) was used for NIR-I imaging. An optical filter (FEL0850, Thorlabs) was adapted with the lens of the camera through an adaptor. Besides, a cooled InGaAs charge-coupled camera (NIRvana: 640, Teledyne Princeton Instruments) was time-division multiplexing and used for NIR-II/IIa/IIb imaging at different times. A cage filter wheel (CFW6/M, Thorlabs) containing three optical filters (FELH1000, Thorlabs; #87-866, Edmund; FELH1500, Thorlabs) was assembled with the lens of the InGaAs camera through an adaptor. The NIR-II/IIa/IIb imaging was spectral un-mixing, which was achieved by switching the three optical filters, respectively. The switching time between two optical filters was within 1 s. Besides, a light source with adjustable power was equipped to provide illumination in the near-infrared spectrum. The laser excitation device included an 808 nm laser generator with a maximum power of 50 w, a beam expander, and an optical fiber. It was convenient to move the whole instrument in the operating room ([Fig. 1\(c\)](#)). Additionally, the costs of the ProEM-HS: 1024BX3 camera, the NIRvana: 640 camera, and the laser excitation device were 67500 \$, 120000 \$, and 7600 \$, respectively.

Additionally, an image fusion method was developed to quickly fuse the acquired images intraoperatively. First of all, to remove the background of the vascular fluorescence images, the U-Net network [27] which was trained in advance based on the DRIVE dataset [28] was used to segment these images. Tensorflow 1.12.0 and Keras 2.2.4 on Python 3.6 were used to train the network, which was implemented on a computer with Ubuntu 16.04 system, Inter Core i7-6500U CPU, and an NVidia GTX 1080Ti GPU. The raw fluorescence images were input into the network and the binary segmented images were produced in which the pixel of vessels was 1 and that of the background was 0. Because the DRIVE dataset was based on vascular images of the retina which was different from the cerebrovascular images in this study, the Canny algorithm [29] was then applied to modify the network's segmentation results. In detail, the binary images generated by the U-Net network and Canny algorithm were fused by OR operation at the corresponding pixel to generate the

TABLE I
DETAILED INFORMATION OF THE IMAGING COMPONENTS AND PARAMETERS

Imaging subsystem	Fluorescence camera type	ProEM-HS: 1024BX3, Teledyne Princeton Instruments	NIRvana: 640, Teledyne Princeton Instruments		
	Spectrum	NIR-I	NIR-II	NIR-IIa	NIR-IIb
	Filter type	FEL0850, Thorlabs	FELH1000, Thorlabs	#87-866, Edmund	FELH1500, Thorlabs
	Filters' spectral responses range (nm)	> 850	> 1000	1300-1350	> 1500
	Exposure time (ms)	50 / 100	20 / 50 / 100	1000	3000
	Frame rates (fps)	4400		110	
	Imaging resolution (μm)	92		62.5	
	Analog to digital conversion speed (MHz)	30		2	
	Lens	VHF 35M-MP SWIR, Spacecom	SWIRON 2.8/50, Schneider Kreuznach		
	Image acquisition software	LightField, Teledyne Princeton Instruments			
	Bit depth (bits)	16			
	File format	*.spe			
	Aperture value	f/2.8			
	Binning	No binning			
Illumination spectrum (nm)	~ 750-1300				
Illumination power (w)	2.5				
Excitation subsystem	Laser power at the imaging site (mW/cm^2)	5 / 50	5 / 50	100	100
	Excitation wavelength (nm)	808			
	Beam expander	Customized, made of a spherical glass, beam divergence 18 mrad			
	Laser fiber	Liquid core optical fiber			

final segmented vessel images. The above-mentioned procedure was integrated into an interactive program to quickly provide segmented images intraoperatively. For the fluorescence images of tumors, background subtraction was performed. The background was defined as the surrounding normal brain tissue. Besides, for the visible light images of the surgical area, brightness and contrast adjustment were performed to get sharper images. Finally, the segmented fluorescence images of vessels, processed fluorescence images of tumors, and processed visible light images of the surgical area were fused using ImageJ (1.8.0_112, National Institutes of Health, USA) in which tumor, arteries, and veins were displayed in green, red, and blue, respectively. The whole image fusion method was deployed on a computer with Windows 10 system, Inter Core i7-6500U CPU, and an NVidia GTX 1080Ti GPU.

B. Multispectral Fluorescence Imaging of Capillary Tube

To compare the scattering property of photons in different spectra, the high scattering Intralipid solution and a capillary tube filled with ICG were used to mimic the brain tissue and cerebral vessels.

The 20% Intralipid solution was diluted to a concentration of 2% using saline. ICG was dissolved in fetal bovine serum to a concentration of 0.01 mg/ml and filled into the capillary tube that with a mean inner diameter of 1 mm. Then the capillary tube was placed in a container and the Intralipid was used to submerge it. Fluorescence imaging was performed along with the capillary tube slowly submerged by the Intralipid solution. The working distance of the cameras was set to 20 cm. The exposure time for NIR-I/II/IIa/IIb imaging was 5 ms, 20 ms, 1 s, and 3 s, respectively. The laser power density at the imaging site for NIR-I/II/IIa/IIb imaging was 5 mW/cm^2 , 5 mW/cm^2 , 100 mW/cm^2 , and 100 mW/cm^2 , respectively.

TABLE II
CHARACTERISTICS AND PREOPERATIVE DIAGNOSIS OF PATIENTS WITH GRADE III/IV GLIOMAS

Variable	Value
Patients (n)	7
Age / year, (M, range)	45 (35-65)
Gender (n)	
Male	3
Female	4
Affected side (n)	
Left	2
Right	4
Diffuse	1
Tumor size (cm^3 , M, range)	36.0 (20.3-47.1)
Tumor depth (cm, M, range)	0.18 (0.00-1.00)
Pre-KPS (M, range)	90 (70-90)
Pre-NIHSS (M, range)	1 (0-3)

M = Median; Pre-KPS = Preoperative Karnofsky Performance Scale; Pre-NIHSS = Preoperative National Institute of Health Stroke Scale.

C. Patient Recruitment and Characteristics

From September to October 2019, seven patients with grade III/IV glioma from Beijing Tiantan Hospital were enrolled (Table II). Inclusion criteria were that patients were 18-75 years old, were diagnosed with grade III/IV glioma by enhanced magnetic resonance imaging (MRI), had only one solid contrast-enhanced lesion detected by MRI, were suitable for tumor resection, had Karnofsky Performance Scale over 70, met the follow-up criteria, and signed informed consent. Exclusion criteria were that patients had a severe allergy to ICG or iodine, any labile systemic disease, suffered from human immunodeficiency virus or liver disease, pregnancy or breastfeeding, and participated in other clinical trials in the past 30 days. The study was approved by the Ethics Committee of Beijing Tiantan

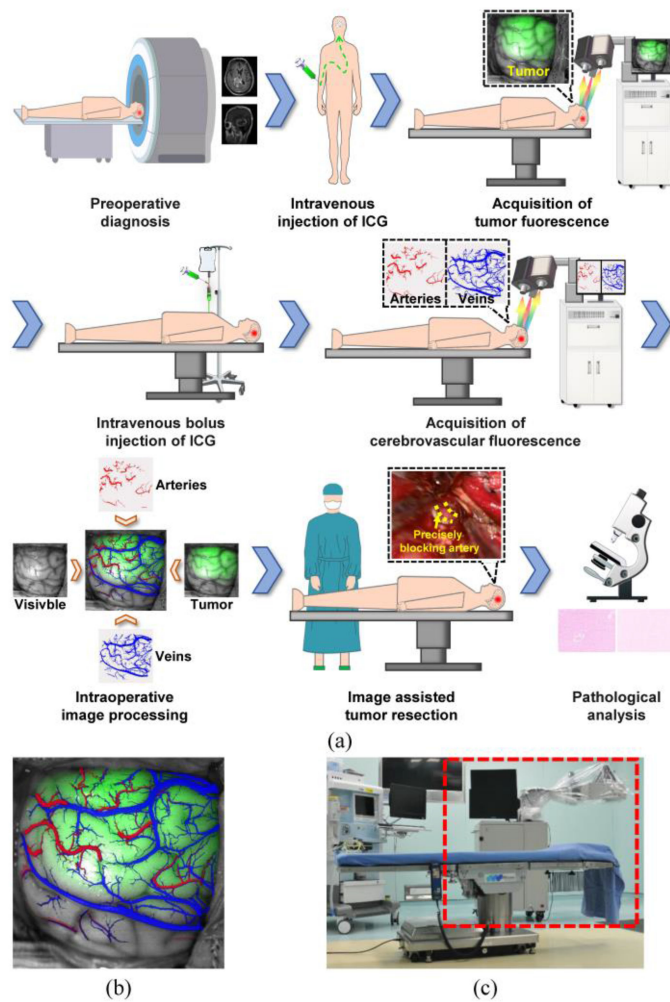


Fig. 1. Description of the clinical protocol and the multispectral fluorescence imaging instrument. (a), Patients first received enhanced MRI examination within 3 weeks before surgery, and those who met the criteria were enrolled. ICG with a dose of 1 mg/kg body weight was injected through the forearm vein 48 hours before surgery. On the day of surgery, images were acquired after opening the dura mater, then ICG (2.5 mg/ml, 10 ml) was administered through intravenous bolus injection and the multispectral fluorescence imaging (NIR-I, NIR-II, NIR-IIa, NIR-IIb) of arteries and veins was performed about 5 s after ICG administration. Subsequently, the acquired images were fused and tumors were resected under the guidance of the fused images. After resection, resected lesions received the pathological examination. (b), An example of the intraoperative fused image. (c), The instrument showed in the red rectangle was placed next to the operation bed before surgery.

Hospital, Capital Medical University, and it was registered at the Chinese Clinical Trial Registry (ChiCTR2000029402).

Besides, other fifteen patients with grade III/IV glioma who underwent tumor resection during the study were also retrospectively enrolled (Table S1), which was set as the control group that only be used to demonstrate the effect of multispectral fluorescence imaging on precisely blocking feeding arteries. The inclusion criteria of the fifteen patients were that the tumor was resected by the same neurosurgeon as the above seven patients, the distribution of patients' age, tumor size, and tumor depth were consistent with the above seven patients. Exclusion criteria were that patients had a recurrence or multiple tumors.

D. Clinical Protocol

Patients first received enhanced MRI examination (Supplementary S1) within 1 week before surgery. ICG (Dandong Yichuang Pharmaceutical Co., Ltd, China) was injected through the forearm vein 48 hours before surgery, and the dose was 1 mg/kg body weight. After injection, any adverse reactions to ICG injection were measured in detail. During the surgery of the patients, visible light, NIR-I, and NIR-II images of the tumor sites were acquired after dural opening. The working distance of the cameras and the beam expander of the excitation subsystem was adjusted to 50 cm. The typical exposure time for NIR-I/II imaging was 50 ms and the laser power density at the imaging site was 50 mW/cm². Subsequently, ICG (2.5 mg/ml, 10 ml) was administered by intravenous bolus injection within 5-10 s. As the route of ICG in the brain is from arteries to capillaries then to veins, the fluorescence appeared in arteries and veins at different time points. The multispectral fluorescence images of arteries and veins were acquired sequentially. The typical exposure time for NIR-I/II/IIa/IIb imaging was 50 ms, 50 ms, 1 s, and 3 s, respectively. Since the signal intensity of ICG in the NIR-IIa/IIb spectra is weak, a long exposure time was necessary. The laser power density at the imaging site for NIR-I/II imaging was 5 mW/cm², and that for NIR-IIa/IIb imaging was 100 mW/cm². Then, the acquired fluorescence images of arteries and veins were segmented and fused with the NIR-II image of the tumor, and the visible light image of the surgical area (Fig. 1(b)). Finally, tumor-feeding arteries blocking and tumor resection were conducted under the guidance of the fused images. Images under white light illumination were also acquired by the surgical microscope alongside the surgery. After resection, the excised tissue was subjected to pathological examination using hematoxylin and eosin staining (Fig. 1(a)). Enhanced MRI examination was then performed 48-72 hours after surgery to measure the residual tumor volume.

E. Analysis of Fluorescence Images and Statistical Analysis

The fluorescence intensity was extracted using ImageJ. The pseudo color of the fluorescence images displayed in each figure was converted using ImageJ. The full width half maximum (FWHM) of Gaussian fitting to the cross-sectional intensity profile was used to calculate the apparent width of the corresponding vessel [30], and the calculation was completed by the Origin software (OriginPro 2018C, OriginLab). The signal-to-background ratio (SBR) of vessels was defined as the division of the mean signal intensity of the vessel and that of the background. The value of the background was the mean signal intensity on both sides of the vessel. And the mean vascular SBR in each spectrum of a patient was defined as the mean value extracted from five different vessels. The SBR of tumors was defined as the division of the mean signal intensity of the tumor and that of the surrounding normal brain tissue. The *t-test* was performed to assess the difference of SBR value between two fluorescence spectra, and the difference of characteristics of patients in two groups. Clinical data were expressed as median and range.

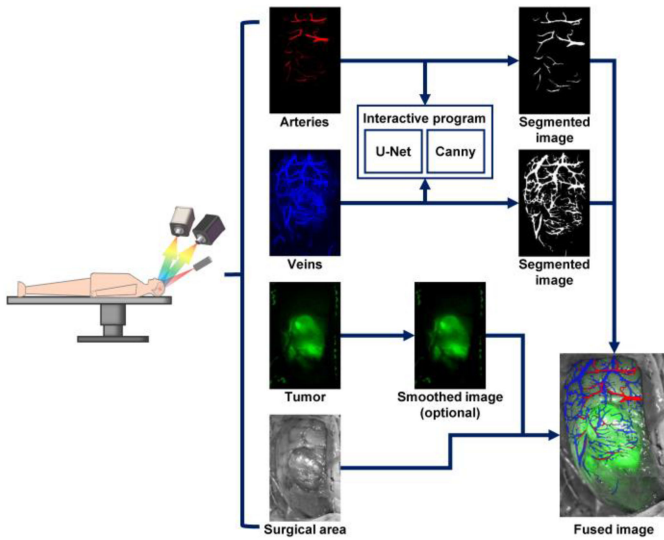


Fig. 2. Schematic of the intraoperative image fusion method.

III. RESULTS

A. NIR-I/II/IIa/IIb Multispectral Imaging Instrument and Image Fusion Method

To apply the NIR-IIa/IIb imaging to glioma resection and assess the effectiveness of this novel technology, a multispectral imaging instrument integrated NIR-I/II/IIa/IIb imaging was constructed, and a corresponding image fusion method was developed. The imaging instrument consisted of an imaging subsystem and a laser excitation subsystem. Detailed information of components and parameters of the instrument was described in Table I. The image fusion method mainly divided into four steps (Fig. 2): Build the interactive program for image segmentation, which was completed before the study and only needed to be implemented once; Segment the fluorescence images of arteries and veins that the neurosurgeons considered the best quality; Smooth the NIR-II fluorescence image of the tumor (optional); Finally fuse the segmented fluorescence images of vessels, NIR-II image of the tumor, and the visible light image of the surgical area using ImageJ.

To further characterize the developed imaging instrument, a capillary tube filled with ICG that was immersed in the Intralipid solution was first imaged by multispectral fluorescence imaging. The scattering effect was obvious as the depth of Intralipid raised. Gaussian fitting of the same capillary tube proved that the FWHM increased rapidly in the NIR-I and NIR-II imaging compared with NIR-IIa and NIR-IIb imaging. Whereas, since the weak fluorescence intensity, almost no fluorescence signal was detected in the NIR-IIb spectrum when the depth was greater than 6 mm (Fig. 3(a)). Specifically, when the depth of Intralipid raised to 5 mm, although the fluorescence was captured in all four spectra, the most serious scattering was observed in the NIR-I spectrum (Fig. 3(b)). Gaussian fitting further proved the lower FWHM of the same capillary tube was obtained in the longer wavelength. The FWHM in the NIR-IIb spectrum was only 1.13 mm, which indicated almost no photons scattering occurred in this spectrum (Fig. 3(c)).

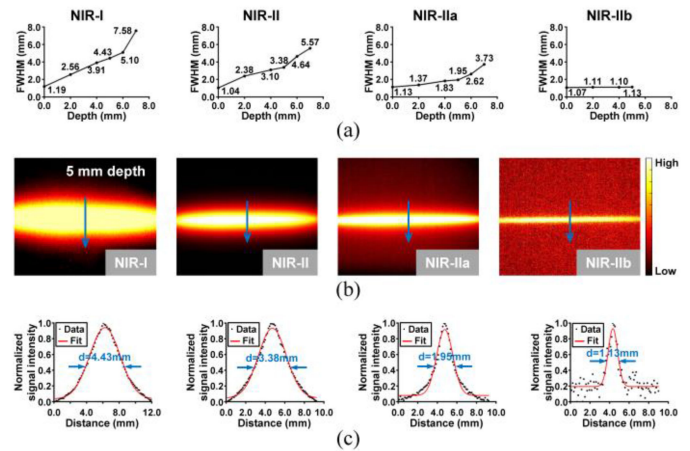


Fig. 3. Comparison of multispectral fluorescence imaging of the same capillary tube. (a), The trends of FWHM of the same capillary tube changes with different Intralipid depth in NIR-I/II/IIa/IIb fluorescence images. (b), Fluorescence images of the capillary tube in each spectrum when the depth of Intralipid raised to 5 mm. Visually, the highest scattering is found in the NIR-I spectrum. (c), Gaussian fitting of the signal intensity profile, which corresponds to the position and direction of the blue rows in b. The FWHM of the same capillary tube in each spectrum is 4.43 mm, 3.38 mm, 1.95 mm, and 1.13 mm, respectively. Abbreviations: d, diameter.

B. Simultaneous Intraoperative Imaging of Glioma and Cerebral Vessels of Patients With Glioma Using Multispectral Fluorescence

For a typical patient in the study, the preoperative MRI of the patient's brain displayed a lesion in the right parietal (Fig. 4(a)), and the diagnosis was malignant glioma. After opening the dura mater, the surgical boundaries and distribution of tumor-feeding arteries were difficult to be identified by surgeons (Fig. 4(b)). Contrastively, the boundaries were distinct in the fluorescence images, in which the SBR was 3.30 in the NIR-II imaging (Fig. 4(c)) and only 1.32 in the NIR-I imaging (Supplementary Fig. S1a). Approximately 10 s post-injection of ICG, fluorescence in the feeding arteries was observed through the NIR-IIb channel (Fig. 4(d)). About 15 s post-injection, fluorescence started to be detected in the smaller veins and then in the larger veins (Fig. 4(e)). For the present patient, six feeding arteries were identified and blocked under the guidance of the fused image (Fig. 4(g)), corresponding to the vessels labeled as 1-6 in Fig. 4(f), respectively. The duration of surgery was 300 min and the blood loss volume was 300 ml, of which the blood loss volume was only 200 ml during tumor removal. After resection, pathological examination revealed that the resected lesion was glioblastoma, with enhanced MRI confirming that the tumor was maximally removed (Fig. 4(h)).

Patients in the fluorescence navigation group who underwent image-guided arteries blocking and tumor resection all followed the clinical protocol described above (Supplementary Fig. S2, Fig. S3). No adverse reactions were recorded after injection of ICG. The postoperative MRI examination demonstrated the tumors were maximally resected for the patients involved, except for a patient whose tumor invaded into the contralateral hemisphere, the maximum extent of resection was achieved on

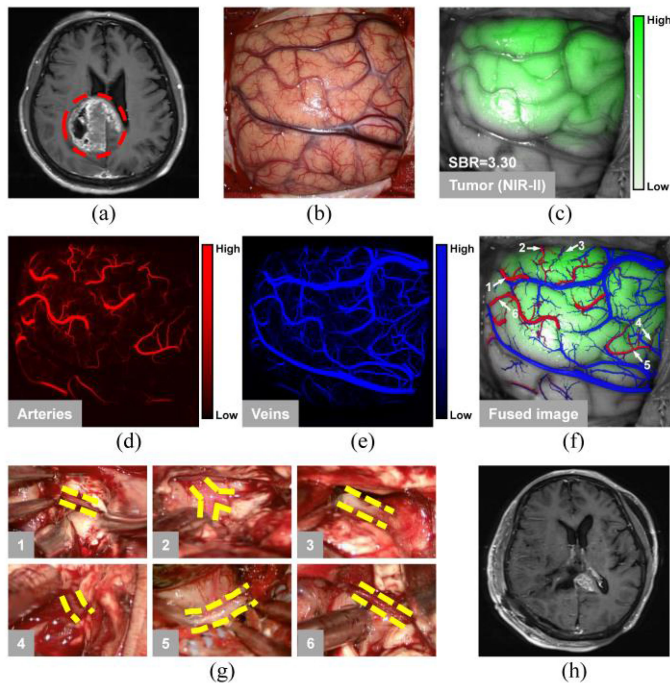


Fig. 4. Image-guided feeding arteries blocking and tumor resection of a patient with GBM. (a), Enhanced MRI examination before surgery, red circle indicates a lesion in the right parietal. (b), Visible light image after dural opening. (c), NIR-II image of the tumor site in which the fluorescence of tumor is shown in green, the SBR of the tumor is 3.30. (d), NIR-IIb image of the feeding arteries. (e), NIR-IIb image of veins that was acquired 2 min post-injection of ICG. (f), Fused image of the tumor, arteries, and veins, which are displayed in green, red, and blue, respectively. White arrows 1–6 correspond to the location of the tumor-feeding arteries. (g), Yellow dotted lines indicate the feeding arteries blocked during tumor resection. Panel 1–6 correspond to the vessels labeled as 1–6 in f. (h), Enhanced MRI examination after surgery indicates the tumor was resected to the maximum extent.

the surgical site. The overall perioperative and pathological data of each patient were summarized in Table III and Supplementary Table S2. No major bleeding occurred during tumor resection. The median duration of the whole surgery and tumor resection was 390 min (range 300-480 min) and 162 min (120-240 min), respectively. The median blood loss volume during surgery and tumor resections were 300 ml (standard deviation: 258.73 ml, range: 200-1000 ml) and 200 ml (standard deviation: 144.82 ml, range: 150-600 ml), respectively.

Different surgical parameters were further compared with those in the control group (Table IV). A patient who underwent fluorescence navigation surgery was excluded for comparison, since the large tumor was diffuse and invaded into the contralateral hemisphere which significantly increased the difficulty of resection. There was no significant difference in gender, age, tumor size, tumor depth, duration of surgery between patients in the two groups. Whereas, the blood loss volume of patients who underwent fluorescence navigation surgery was significantly reduced versus the control group ($p = 0.0366$). Clinical results demonstrated the effect of multispectral fluorescence imaging on precisely blocking the feeding arteries.

TABLE III
SURGICAL AND PATHOLOGICAL DATA OF EACH PATIENT

Variable	Value
Duration of surgery (min, M, range)	390 (300-480)
Duration of tumor resection (min, M, range)	162 (120-240)
Blood loss during surgery (ml, M, range)	300 (200-1000)
Blood loss during tumor resection (ml, M, range)	200 (150-600)
Extent of resection (M, range)	100% (81.08%-100%)
Progression-free survival (month, M, range)	9 (4-18)
Pathology	
AOG	2
GBM	4
AOA	1
WHO grade	
III	3
III-IV	1
IV	3
3 d. Post-KPS	90 (60-90)
3 d. Post-NIHSS	1 (1-4)

M = Median; AOG = Anaplastic Oligodendroglioma; GBM = Glioblastoma; AOA = Anaplastic Oligoastrocytoma; WHO = World Health Organization; 3 d. Post-KPS = 3 Days Postoperative Karnofsky Performance Scale; 3 d. Post-NIHSS = 3 Days Postoperative National Institute of Health Stroke Scale.

TABLE IV
COMPARISON OF DIFFERENT PARAMETERS IN TWO GROUPS

Characteristics	FN group (n=6)	Control group (n=15)	P value
Sex (Male/Female)	0.5	2.0	0.1799
Age (mean±s.d.)	49.8±7.5	52.8±14.2	0.6502
Tumor size (cm ³ , mean±s.d.)	35.8±8.0	47.6±24.4	0.2843
Tumor depth (cm, mean±s.d.)	0.4±0.4	0.7±1.0	0.5625
Duration of surgery (min, mean±s.d.)	375.0±64.2	368.0±78.8	0.8559
Blood loss during surgery (ml, mean±s.d.)	283.3±68.7	453.3±170.8	0.0366

FN = Fluorescence Navigation.

C. Visualization and Noninvasive Quantification of the Blood Flow in Patients' Cerebral Vessels

For a female patient, NIR-II imaging of the blood flow was performed at a frame rate of 50 fps immediately after intravenous bolus injection of ICG (Video S1). About 10 s after injection of ICG, the NIR-II signal was observed in the feeding arteries of the tumor (Fig. 5(a)). And $t = 0$ s was defined as the time when the NIR-II signal started to appear in the vessels. The perfusion direction of fluorescence in some arteries was also recorded (indicated by the white arrow in Fig. 5(a)). At $t = 1.8$ s, the fluorescence was observed returning from the arteries through the small veins back to the adjacent main veins. And $t = 3.6$ s, fluorescence was detected in all vessels (Fig. 5(b)). In the arteries, the normalized fluorescence intensity exponentially raised as time increases (Fig. 5(c)). The position where the signal intensity was extracted in different time point were kept the same (as shown by the blue rectangle in the eighth panel of Fig. 5(a)). Specifically, the correlation between signal intensity and time was $I = -0.24 + 0.18e^{\frac{t}{507}}$ ($R^2 = 0.99$). Similarly,

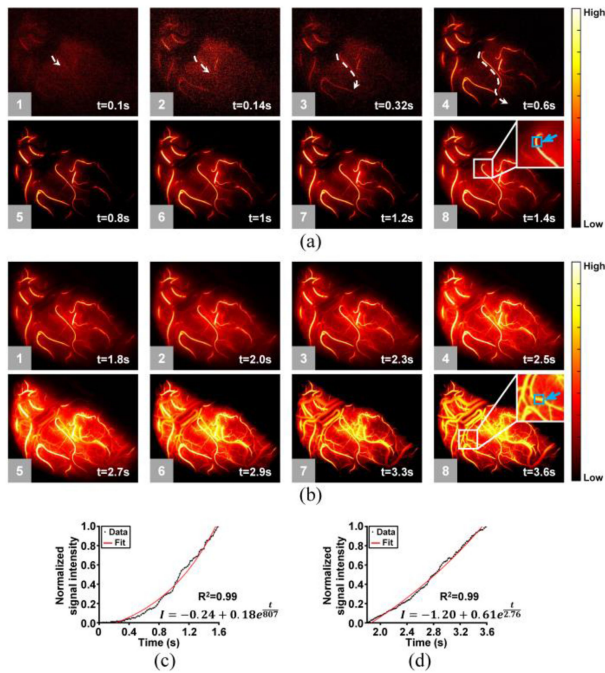


Fig. 5. Real-time blood flow imaging of a female patient in the NIR-II spectrum. (a), NIR-II images of feeding arteries after injecting ICG, white arrows show the blood flow of an artery. (b), NIR-II images of drainage veins. (c), The dots indicate the normalized signal intensity of an artery, and the red fitting line demonstrates the signal intensity increased exponentially. (d), Black dots indicate the normalized signal intensity of a vein. The red fitting line also indicates the signal intensity displayed an exponential increase.

the signal intensity in the veins also featured an exponential increase (Fig. 5(d)), and the position where the signal intensity was extracted was shown by the blue rectangle in the eighth panel of Fig. 5(b). The exponential fitting formula was found to be $I = -1.20 + 0.61e^{0.27t}$ ($R^2 = 0.99$).

Besides, a male patient underwent NIR-I imaging at a frame rate of 10 fps after injecting ICG for comparison with NIR-II imaging. The imaging contrast of feeding arteries and veins in the NIR-I spectrum was not as obvious as that in the NIR-II imaging since the high background noise (Fig. S4a, b; Video S2). The normalized signal intensity in a typical artery and vein linearly increased with the injection time (artery: $I = -0.04 + 9.10 \times 10^{-4}t$, $R^2 = 0.98$; vein: $I = -0.51 + 0.45t$, $R^2 = 0.95$) (Fig. S4c, d). Compared with the blood flow imaging in the two spectra, the background noise of NIR-II imaging was obviously lower than that of the NIR-I imaging.

D. NIR-IIb Imaging of Cerebral Vessels in High Performance

For the seven enrolled patients who underwent NIR-I/II imaging during the venous phase, four of them also received NIR-IIa/IIb imaging. Analysis indicated the mean vascular SBR in the longer wavelength was much higher than that in the shorter wavelength for each patient (Fig. 6(a), Supplementary Table S3). Particularly, the mean SBR in the NIR-IIb imaging was even high up to 5.30 ± 2.27 (mean \pm s.d.), which was several folders

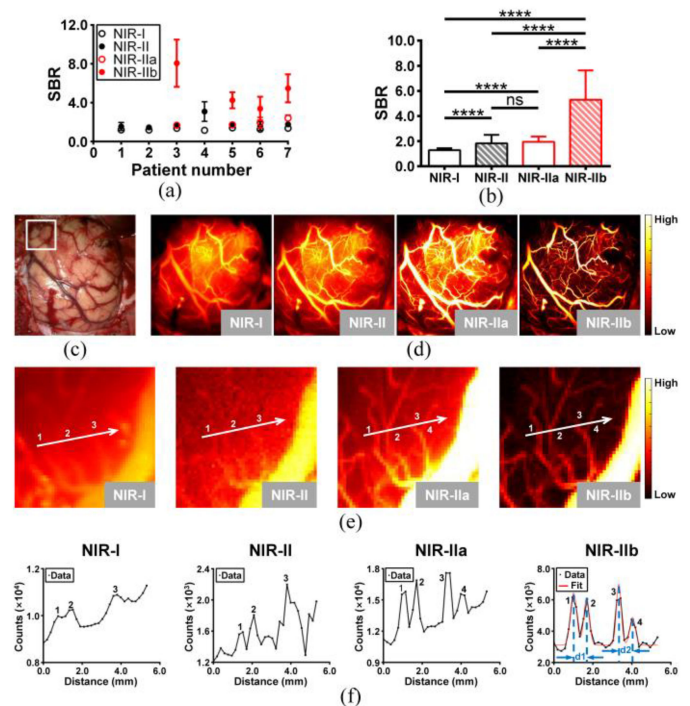


Fig. 6. Comparison of multispectral fluorescence images. (a), Vascular SBR in different spectra of each patient. (b), The mean vascular SBR of the seven patients. (c–d), Visible light and multispectral fluorescence images of cerebral vessels. (e), Fluorescence images of the enlarged view of the white rectangle in c. Three veins are distinguished in the NIR-I and NIR-II imaging while four are distinguished in the NIR-IIa and NIR-IIb imaging. (f), Cross-sectional intensity profiles, which correspond to the location and direction of white arrows in e, respectively. D1 indicated the center distance between vessel 1 and vessel 2, which was 0.67 mm. Similarly, d2 indicated the center distance between vessel 3 and vessel 4, which was 0.71 mm. The *t*-test was used to calculate the significance. ****: $P < 0.0001$, ns: no significance. Data in a and b are presented as mean \pm s.d.

(2.7 - 4.1) of that obtained in other imaging spectra (NIR-I: 1.28 ± 0.15 , NIR-II: 1.82 ± 0.67 , NIR-IIa: 1.95 ± 0.41), ($p < 0.0001$, Fig. 6(b)). Furthermore, the SBR in the NIR-IIa/II spectrum was significantly higher than that in the NIR-I spectrum too ($p < 0.0001$).

Because of the high contrast and less interference from the background fluorescence, a higher spatial resolution was achieved in the imaging with a longer wavelength. For a typical patient with GBM, only superficial vessels were observed after opening the dura mater (Fig. 6(c)). However deeper vessels and microvessels were detected by fluorescence imaging, with more details intuitively exhibited in longer wavelength (Fig. 6(d)). Compared with NIR-I, NIR-II, NIR-IIa, it was obvious that NIR-IIb imaging has the highest contrast and resolution for visualizing the vessels. For the enlarged view of the white rectangle area in Fig. 6(c), NIR-IIb imaging exhibited the sharpest view compared with other spectra, and four drainage veins (indicated as 1 to 4) were detected in the NIR-IIa/IIb spectra. However, blurry scenes were presented in the NIR-I/II spectra with the adjacent two microvessels that were hard to be differentiated. Besides, intense background fluorescence was exhibited in the NIR-IIa spectrum compared with the NIR-IIb imaging (Fig. 6(e)). White

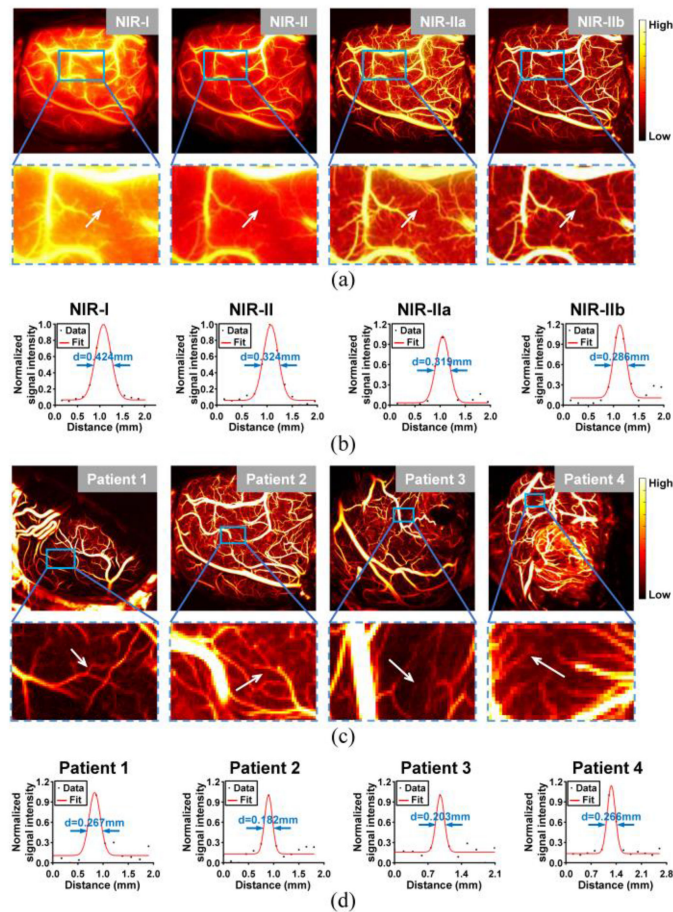


Fig. 7. Capillaries detected in the NIR-IIb spectrum. (a), Multispectral fluorescence images at the venous phase of a patient. (b), Gaussian fitting of the signal intensity profiles, the lowest FWHM value was obtained in the NIR-IIb spectrum. The intensity was extracted from the position of the white arrows in a, respectively. (c), NIR-IIb images at the venous phase of four patients. (d), FWHM of Gaussian fitting in each profile is 0.267 mm, 0.182 mm, 0.203 mm, and 0.266 mm, respectively. The intensity was extracted from the position of the white arrows in c, respectively. Abbreviations: d, diameter.

arrows in Fig. 6(e) corresponded to the location and direction of cross-sectional intensity profiles in Fig. 6(f), respectively. Quantification results also displayed the highest spatial resolution in the NIR-IIb spectrum. Specifically, the apparent diameter of the four vessels was 0.37 mm, 0.34 mm, 0.30 mm, and 0.34 mm, respectively. The center distance between vessel 1 and vessel 2 was 0.67 mm, and that between vessel 3 and vessel 4 was 0.71 mm (Fig. 6(f)).

E. Capillaries Detected in the NIR-IIb Spectrum

Similar to the phantom study, the sharpest vascular network was also acquired in the NIR-IIb images (Fig. 7(a)). Additionally, the FWHM of Gaussian fitting showed that the apparent diameter of the same vessel in the NIR-I spectrum was almost 1.5 times that in the NIR-IIb spectrum (Fig. 7(b); 0.424 mm in NIR-I vs. 0.286 mm in NIR-IIb). Therefore, the NIR-IIb imaging can simultaneously achieve the highest vascular SBR and the lowest photon scattering in patients during surgery,

which is the same as the capillary phantom experiment. And for the four patients who underwent NIR-IIb imaging during the venous phase, the subtlest vascular network was acquired (Fig. 7(c)). The fitting diameter of the thinnest microvessels in each patient was 0.267 mm, 0.182 mm, 0.203 mm, and 0.266 mm, respectively (Fig. 7(d)). NIR-IIb imaging equipped in the novel multispectral fluorescence imaging instrument showed a powerful ability to visualize vessels with a diameter as tiny as 182 μm .

IV. DISCUSSION

In this study, the NIR-IIa/IIb imaging has been successfully used for the resection of grade III/IV glioma. Fluorescence imaging in the longer wavelength over 1300 nm exhibited many advantages in terms of spatial resolution and imaging contrast, etc. Combining the FDA-approved imaging probe ICG, the vascular distribution and surgical boundaries can be simultaneously delineated during surgery. Seven patients with grade III/IV glioma have been enrolled, whose feeding arteries of tumors have been precisely located and blocked. Furthermore, all tumors have been successfully resected without major bleeding with the assistance of this novel technology. Clinical results demonstrate that this multispectral fluorescence imaging is useful for neurosurgeons during glioma resection.

Intraoperative blood loss volume is affected by many factors such as the operator, tumor size, and location. Benefiting from the precise blocking of tumor-feeding arteries, the blood loss volume was significantly smaller than that in the control group ($P = 0.0366$). However, the surgical data of the control group were retrospectively analyzed. Since this is a study mainly describing the novel multispectral fluorescence imaging, no randomized controlled study was performed. In the future, a randomized controlled study is needed to further demonstrate the efficacy of this novel technology used for reducing the blood loss volume. Besides, the median duration of surgery in this study was 390 min, with a median duration of tumor resection to be only 162 min. The time of image segmentation and fusion was less than 1 min, and the whole image process did not significantly prolong the duration of the surgery. However, this is a pilot study that involved the comparison of multispectral fluorescence imaging, multiple fluorescence images of vessels in each spectrum were acquired in each patient. In the future, by simplifying the image acquisition process and reducing the number of images acquired, the duration of the whole surgery can be further shortened.

A real-time fluorescence imaging with a speed of 50 fps in the NIR-II spectrum has been achieved after intravenous administration of ICG, where a distinct blood flow is displayed (Fig. 5(a), (b)). Compared with the conventional fluorescence imaging in the NIR-I spectrum, a higher vascular SBR and lower photon scattering have been attained. These advantages make it a powerful tool to replace the NIR-I imaging that is used for ICG video angiography during cerebrovascular surgery. Additionally, the exponential increase property of fluorescence intensity in vessels in the NIR-II imaging offers a possibility for monitoring and quantitative analysis of the blood perfusion intraoperatively [31]. And the ability to capture the direction

of blood perfusion could be used to analyze the aneurysmal dilation of vessels [32]. Not only multiple vessels have been synchronously tracked under the large field of view in the real-time imaging, but also a contactless imaging method has been provided compared with Doppler measurement. Moreover, the highest vascular SBR and a capillaries resolution of nearly 180 μm have been guaranteed in the NIR-IIb spectrum. Therefore, the imaging requirements of high time resolution or high spatial resolution can be simply achieved by the same instrument.

The determination of tumor boundaries and vascular distribution is necessary for accurate vessel blocking. Thus, ICG has been intravenously injected 48 hours before surgery to obtain the tumor fluorescence. The tumor SBR is 1.32 in NIR-I imaging and 3.30 in NIR-II imaging, which is approximately 2.5 times that obtained from NIR-I imaging (Supplementary Fig. S1). Therefore, the fluorescence image of tumors in the NIR-II spectrum has been used to fuse. Although high tumor SBR has been found, the fluorescence intensity in both NIR-I/II spectra is much lower than that of the vessels during angiography. Additionally, tumors have been found to show almost no fluorescence in the NIR-IIb spectrum (Supplementary Fig. S2c). Therefore, the intense fluorescence from vessels provides a high imaging contrast that is hardly affected by the surrounding negligible tumor fluorescence especially using the NIR-IIb imaging. Thus, considering the highest performance exhibited in the NIR-IIb imaging, tumor fluorescence in the NIR-II spectrum and vascular fluorescence in the NIR-IIb spectrum is the best choice for image fusion.

The signal intensity turned weaker in the longer wavelength, owing to the tailing character of ICG in the emission spectrum over 1000 nm [13]. A typical example was shown in the NIR-IIb image of Fig. 3(b). The fluorescence intensity was relatively low and a large background component was included when the depth of Intralipid raised to 5 mm. Therefore, an exposure time of 3 s has been used to capture adequate photons in the NIR-IIb spectrum. Whereas, since the transient duration of the arterial phase, only up to two fluorescence images could be acquired. Although the highest contrast has been obtained, the long exposure time made it impossible to provide real-time imaging like that in the NIR-II spectrum.

To the best of our knowledge, it is for the first time to apply the NIR-IIa/IIb imaging to clinical use. Using the multispectral fluorescence imaging instrument and image fusion method, vessels around the tumor can be blocked precisely. It not only effectively avoids the extended resection which is usually used to stanch, but also reduces the incidence of damage to normal brain tissue and normal vessels. Furthermore, the novel NIR-IIa/IIb imaging technology can be a powerful tool for image-guided resection of glioma. It can be an alternative tool for existing angiography methods. Additionally, combined with other technologies, the multispectral fluorescence imaging is expected to play a greater role in future image-guided surgery [33]–[36].

V. CONCLUSION

In this study, the NIR-IIa/IIb imaging has been successfully used to precisely resect grade III/IV glioma, their outstanding

performance has been proved for the first time in the clinic. All tumors were resected to the maximum extent and the blood loss volume was dramatically decreased. Additionally, the real-time imaging of blood flow in the NIR-II spectrum and the high spatial resolution in the NIR-IIb spectrum exhibits the power of multispectral fluorescence imaging.

REFERENCES

- [1] Z. Hu *et al.*, “NIRF nanoprobe for cancer molecular imaging: Approaching clinic,” *Trends Mol. Med.*, vol. 26, no. 5, pp. 469–482, May 2020.
- [2] J. Yang *et al.*, “In vivo multifunctional fluorescence imaging using liposome-coated lanthanide nanoparticles in near-infrared-II/IIa/IIb windows,” *Nano Today*, vol. 38, Jun. 2021, Art. no. 101120.
- [3] Z. Hu *et al.*, “In vivo 3-dimensional radiopharmaceutical-excited fluorescence tomography,” *J. Nucl. Med.*, vol. 58, no. 1, pp. 169–174, Jan. 2017.
- [4] M. Cai *et al.*, “NIR-II/NIR-I fluorescence molecular tomography of heterogeneous mice based on gaussian weighted neighborhood fused lasso method,” *IEEE Trans. Med. Imag.*, vol. 39, no. 6, pp. 2213–2222, Jun. 2020.
- [5] C. Cao *et al.*, “Intraoperative near-infrared II window fluorescence imaging-assisted nephron-sparing surgery for complete resection of cystic renal masses,” *Clin. Transl. Med.*, vol. 11, no. 10, Oct. 2021, Art. no. e604.
- [6] Z. Hu *et al.*, “Nanoparticle-mediated radiopharmaceutical-excited fluorescence molecular imaging allows precise image-guided tumor-removal surgery,” *Nanomedicine*, vol. 13, no. 4, pp. 1323–1331, May 2017.
- [7] Y. Duan and B. Liu, “Recent advances of optical imaging in the second near-infrared window,” *Adv. Mater.*, vol. 30, no. 47, Nov. 2018, Art. no. 1802394.
- [8] G. Hong, A. L. Antaris, and H. Dai, “Near-infrared fluorophores for biomedical imaging,” *Nature Biomed. Eng.*, vol. 1, no. 1, pp. 1–22, Jan. 2017.
- [9] Y. Li *et al.*, “Design of AIEgens for near-infrared IIb imaging through structural modulation at molecular and morphological levels,” *Nature Commun.*, vol. 11, no. 1, pp. 1–10, Mar. 2020.
- [10] S. Diao *et al.*, “Fluorescence imaging in vivo at wavelengths beyond 1500 nm,” *Angew. Chem. Int. Ed. Engl.*, vol. 54, no. 49, pp. 14758–14762, Dec. 2015.
- [11] Z. Ma *et al.*, “Near-infrared IIb fluorescence imaging of vascular regeneration with dynamic tissue perfusion measurement and high spatial resolution,” *Adv. Funct. Mater.*, vol. 28, no. 36, Sep. 2018, Art. no. 1803417.
- [12] S. Wang *et al.*, “In vivo high-resolution ratiometric fluorescence imaging of inflammation using NIR-II nanoprobe with 1550 nm emission,” *Nano Lett.*, vol. 19, no. 4, pp. 2418–2427, Apr. 2019.
- [13] A. L. Antaris *et al.*, “A high quantum yield molecule-protein complex fluorophore for near-infrared II imaging,” *Nature Commun.*, vol. 8, no. 1, pp. 1–11, May 2017.
- [14] J. A. Carr *et al.*, “Shortwave infrared fluorescence imaging with the clinically approved near-infrared dye indocyanine green,” *Proc. Natl. Acad. Sci. U. S. A.*, vol. 115, no. 17, pp. 4465–4470, Apr. 2018.
- [15] Z. Hu *et al.*, “First-in-human liver-tumour surgery guided by multispectral fluorescence imaging in the visible and near-infrared-I/II windows,” *Nature Biomed. Eng.*, vol. 4, no. 3, pp. 259–271, Mar. 2020.
- [16] Q. T. Ostrom *et al.*, “Adult glioma incidence and survival by race or ethnicity in the United States from 2000 to 2014,” *JAMA Oncol.*, vol. 4, no. 9, pp. 1254–1262, Sep. 2018.
- [17] K. Chang *et al.*, “Residual convolutional neural network for the determination of IDH status in low- and high-grade gliomas from MR imaging,” *Clin. Cancer Res.*, vol. 24, no. 5, pp. 1073–1081, Mar. 2018.
- [18] I. Y. Eyupoglu *et al.*, “Surgical resection of malignant gliomas-role in optimizing patient outcome,” *Nature Rev. Neurol.*, vol. 9, no. 3, pp. 141–151, Mar. 2013.
- [19] P. Jia *et al.*, “Long non-coding RNA H19 regulates glioma angiogenesis and the biological behavior of glioma-associated endothelial cells by inhibiting microRNA-29a,” *Cancer Lett.*, vol. 381, no. 2, pp. 359–369, Oct. 2016.
- [20] M. Ameratunga *et al.*, “Anti-angiogenic therapy for high-grade glioma,” *Cochrane Database Syst. Rev.*, vol. 11, Nov. 2018, Art. no. CD008218.
- [21] A. Lopez-Gonzalez *et al.*, “Association between cerebral infarction and malignant glioma,” *Rev. Neurol.*, vol. 40, no. 1, pp. 34–37, Jan. 2005.
- [22] M. K. Ghosh *et al.*, “The interrelationship between cerebral ischemic stroke and glioma: A comprehensive study of recent reports,” *Signal Transduct. Target. Ther.*, vol. 4, no. 1, pp. 1–13, Oct. 2019.

- [23] S. Marbacher *et al.*, "Comparison of 3D intraoperative digital subtraction angiography and intraoperative indocyanine green video angiography during intracranial aneurysm surgery," *J. Neurosurg.*, vol. 131, no. 1, pp. 64–71, Jul. 2018.
- [24] S. Khan *et al.*, "Meningeal contribution to migraine pain: A magnetic resonance angiography study," *Brain*, vol. 142, pp. 93–102, Jan. 2019.
- [25] M. P. Garrett *et al.*, "Computed tomography angiography as a confirmatory test for the diagnosis of brain death," *J. Neurosurg.*, vol. 128, no. 2, pp. 639–644, Feb. 2018.
- [26] H. J. Yi *et al.*, "Analysis of radiation doses and dose reduction strategies during cerebral digital subtraction angiography," *World Neurosurg.*, vol. 100, pp. 216–223, Apr. 2017.
- [27] O. Ronneberger, P. Fischer, and T. Brox, "U-Net: Convolutional networks for biomedical image segmentation," *Med. Image Comput. Comput.-Assist. Intervention*, vol. 9351, pp. 234–241, 2015.
- [28] J. Staal *et al.*, "Ridge-based vessel segmentation in color images of the retina," *IEEE Trans. Med. Imag.*, vol. 23, no. 4, pp. 501–509, Apr. 2004.
- [29] J. Canny, "A computational approach to edge-detection," *IEEE Trans. Pattern Anal. Mach. Intell.*, vol. 8, no. 6, pp. 679–698, Nov. 1986.
- [30] M. Zhang *et al.*, "Bright quantum dots emitting at $\sim 1,600$ nm in the NIR-IIb window for deep tissue fluorescence imaging," *Proc. Natl. Acad. Sci. U. S. A.*, vol. 115, no. 26, pp. 6590–6595, Jun. 2018.
- [31] G. Hong *et al.*, "Through-skull fluorescence imaging of the brain in a new near-infrared window," *Nature Photon.*, vol. 8, no. 9, pp. 723–730, Sep. 2014.
- [32] G. Hong *et al.*, "Multifunctional in vivo vascular imaging using near-infrared II fluorescence," *Nature Med.*, vol. 18, no. 12, pp. 1841–1846, Dec. 2012.
- [33] W. Si *et al.*, "Assessing performance of augmented reality-based neurosurgical training," *Visual Comput. Ind., Biomed.*, vol. 2, no. 1, pp. 1–10, Jul. 2019.
- [34] Y. Liu *et al.*, "Optical focusing deep inside dynamic scattering media with near-infrared time-reversed ultrasonically encoded (TRUE) light," *Nature Commun.*, vol. 6, no. 9, pp. 1–9, Jan. 2015.
- [35] Y. Luo *et al.*, "Towards smart optical focusing: Deep learning-empowered dynamic wavefront shaping through nonstationary scattering media," *Photon. Res.*, vol. 9, no. 8, pp. B262–B278, Aug. 2021.
- [36] P. Lai *et al.*, "Photoacoustically guided wavefront shaping for enhanced optical focusing in scattering media," *Nature Photon.*, vol. 9, no. 2, pp. 126–132, Feb. 2015.